O-Doped Nanographenes: The Pyrano/Pyrylium Route Towards Semiconducting Cationic Mixed-Valence Complexes

*Luka Đorđević, Cataldo Valentini, Nicola Demitri, Cécile Mézière, Magali Allain, Marc Sallé, Andrea Folli, Damien Murphy, Samuel Mañas-Valero, Eugenio Coronado, and Davide Bonifazi**

Abstract: *Herein we report an efficient synthesis to prepare O-doped nanographenes derived from the π-extension of pyrene. The derivatives are highly fluorescent and feature low oxidation potentials. Using electrooxidation, crystals of cationic mixed-valence (MV) complexes were grown in which the organic salts organize into face-to-face π-stacks, a favorable solid-state arrangement for organic electronics. Variable-temperature electron paramagnetic resonance (EPR) measurements and relaxation studies suggest a strong electron delocalization along the longitudinal axis of the columnar π-stacking architectures. Electric measurements of single crystals of the MV salts show a semiconducting behavior with a remarkably high conductivity at room temperature. These findings support the notion that π-extension of heteroatom-doped polycyclic aromatic hydrocarbons is an attractive approach to fabricate nanographenes with a broad spectrum of semiconducting properties and high charge mobilities.*

Introduction

The engineering of polycyclic aromatic hydrocarbons (PAHs)[1] for the use as organic-semiconductor materials has recently gathered great attention.[2] Replacing carbon atoms with other isolobal atoms, that is, doping,[3] is emerging as a powerful approach to control the chemical, supramolecular, and optoelectronic properties of PAHs. Recent examples include Period-2 elements like B-,[4] N-,[5] and O-PAHs.[6] Furthermore, the doping of PAHs allows to synthesize structures that are difficult to be prepared without dopants.[7]

Inspired by the chemical structures of natural anthocyanins[8] and artificial π-expanded xanthenium cations,[9] we inferred that pyranyl and pyrylium rings[10] could be used to prepare the O-doped derivatives of PAHs $\mathbf{1_C}$–$\mathbf{3_C}$ and to engineer *p*-type organic semiconductors. Out of the three PAHs $\mathbf{1_C}$–$\mathbf{3_C}$ (Figure 1, top), attention has been paid only to dibenzanthanthrene ($\mathbf{1_C}$)[11] and its derivatives,[12] with applications in single-molecule transistors,[13] optical interaction with alkali atoms for quantum memory,[14] as a single emitter for super-resolution microscopy,[15] and semiconductors with high mobility in solution-processed OFETs.[12b]

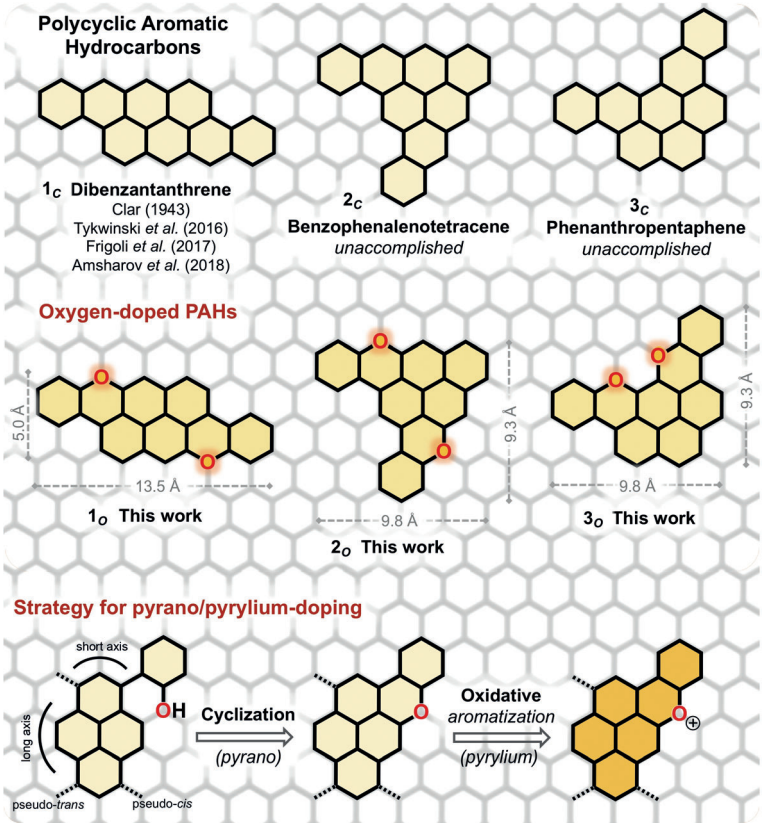

Figure 1. Structural frameworks of all-carbon (top) and O-doped (center) PAHs discussed in this work, along with the synthetic approach (bottom).

[*] Dr. L. Đorđević, C. Valentini, Dr. A. Folli, Prof. Dr. D. Murphy, Prof. Dr. D. Bonifazi
School of Chemistry, Cardiff University, Main Building
Park Place, Cardiff CF10 3AT (UK)
E-mail: bonifazid@cardiff.ac.uk

Dr. N. Demitri
Elettra—Sincrotrone Trieste
S.S. 14 Km 163.5 in Area Science Park, 34149 Basovizza, Trieste (Italy)

C. Mézière, M. Allain, Prof. Dr. M. Sallé
MOLTECH-Anjou—UMR CNRS 6200, UNIV Angers, SFR Matrix
2 Boulevard Lavoisier, 49045 Angers Cedex (France)

S. Mañas-Valero, Prof. Dr. E. Coronado
Instituto de Ciencia Molecular, Universitat de València
Catedrático José Beltrán 2, 46980 Paterna (Spain)

Supporting information and the ORCID identification number(s) for the author(s) of this article can be found under:
https://doi.org/10.1002/anie.201914025.

Building on these precedents, we herein report a robust synthetic approach for the preparation of unprecedented O-doped PAHs $\mathbf{1_O}$–$\mathbf{3_O}$ (Figure 1, middle) in which two carbon atoms have been replaced by oxygen atoms. At the structural level, this entails the replacement of two fused benzene rings by two pyranyl cycles. The resulting structures reflect disubstituted pyrenes (with a long-axis or short-axis substitution pattern, depending on the targeted isomer) with two phenols as key core and peripheral moieties (Figure 1, bottom). To favor solubility, all molecules were decorated with *t*-butyl groups (Scheme 1). Capitalizing on the oxidative Pummerer cyclization[16] of *peri*-xanthenoxanthene (PXX), we expected that this protocol could also lead to isolated pyranyl rings[17] which, in turn, could be oxidized to pyrylium cations (Figure 1, bottom). Interestingly, mixed-valence (MV) complexes could be formed in the solid state between the electron-donating pyranyl molecules and its cationic pyrylium derivatives, generating *p*-type organic semiconductors.

Results and Discussion

We first prepared 1,6-dibromopyrene (**4**) and 1,8-diiodopyrene (**10**) precursors through regioselective bromination (Br_2 in $CHCl_3$) and iodination (I_2 and KIO_3 in $CH_3COOH/H_2O/H_2SO_4$) of pyrene, respectively (Scheme 1).[18] Regarding the 1,3-dibromo isomer (**7**), the pyrenyl core was first mono-*tert*-butylated and then dibrominated with NBS. Suzuki–Miyaura cross-coupling between the relevant dihalide pyrenyl precursor and 4-*tert*-butyl-2-methoxyphenylboronic acid, using $[Pd(PPh_3)_4]$ as a catalyst, gave access to the phenol-bearing pyrenes **6**, **9**, and **12** in excellent yields, after demethylation with BBr_3. A final oxidative Pummerer ring-closure with CuO in $PhNO_2$ under reflux conditions yielded the O-doped PAHs $\mathbf{1_O}$-$\mathbf{3_O}$ in very good yields.

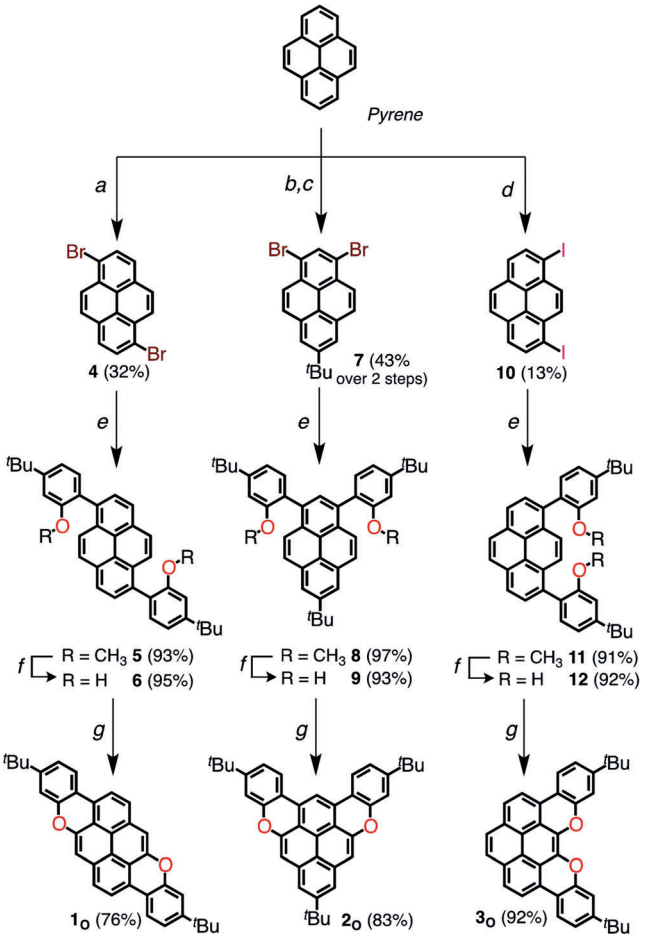

Scheme 1. Synthetic routes to $\mathbf{1_O}$, $\mathbf{2_O}$, and $\mathbf{3_O}$. Reagents and conditions: a) Br_2, $CHCl_3$, rt; b) ^tBuCl, $AlCl_3$, CH_2Cl_2, rt; c) NBS, THF, 30 °C; d) I_2, KIO_3, $CH_3COOH/H_2O/H_2SO_4$, 40 °C; e) 4-*tert*-butyl-2-methoxyphenylboronic acid, $[Pd(PPh_3)_4]$, NaOH, dioxane/H_2O, reflux; f) BBr_3, CH_2Cl_2, 0 °C→rt; g) CuO, $PhNO_2$, reflux.

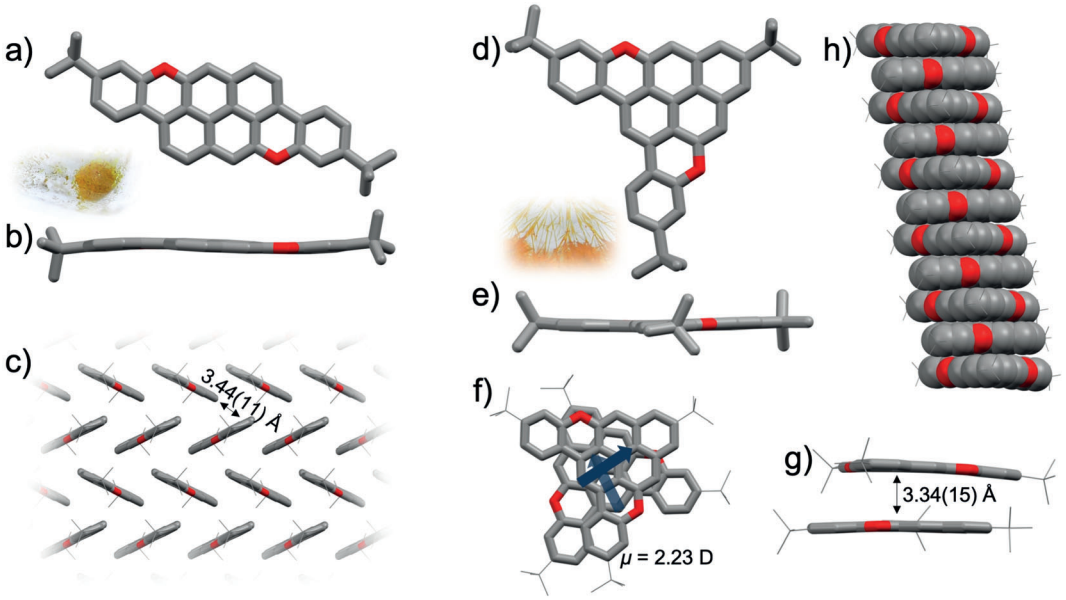

Figure 2. X-ray crystal structures of $\mathbf{1_O}$ and $\mathbf{2_O}$. a) Top view, b) side view, and c) packing mode of $\mathbf{1_O}$. d) Top view, e) side view, and h) packing mode of $\mathbf{2_O}$. f), g) Details related to the stacking mode of $\mathbf{2_O}$, top and side view. Space groups: $P2_1/I$ ($\mathbf{1_O}$) and $C2/c$ ($\mathbf{2_O}$). Atom colors: red (O), gray (C).

Suitable crystals for X-ray diffraction (Figure 2) were prepared by slow evaporation (for $\mathbf{1_O}$) and vapor exchange (for $\mathbf{2_O}$). Attempts to obtain crystals for $\mathbf{3_O}$ failed, and only the X-ray structure of a dichlorinated neutral derivative ($\mathbf{3_OCl_2}$) was obtained after chemical oxidation experiments (Supporting Information, Figures S1 d, S2 d, and S7). In the solid state, molecule $\mathbf{1_O}$ establishes C–H···π interactions in a herringbone arrangement with a distance of 3.45-(11) Å and an angle of ≈50° (Figure 2 c), measured as the distance between the carbon atom and the closest ring centroid, and the angle between the C–H bond and the π-plane (equivalent to the angle between the average aromatic planes of neighboring molecules in the herring-bone structure). Molecule $\mathbf{2_O}$ forms pillars through π-stacks (Figure 2 h,g) with an interplanar distance of 3.34(15) Å and a relative orientation of ≈80° (Figure 2 f).

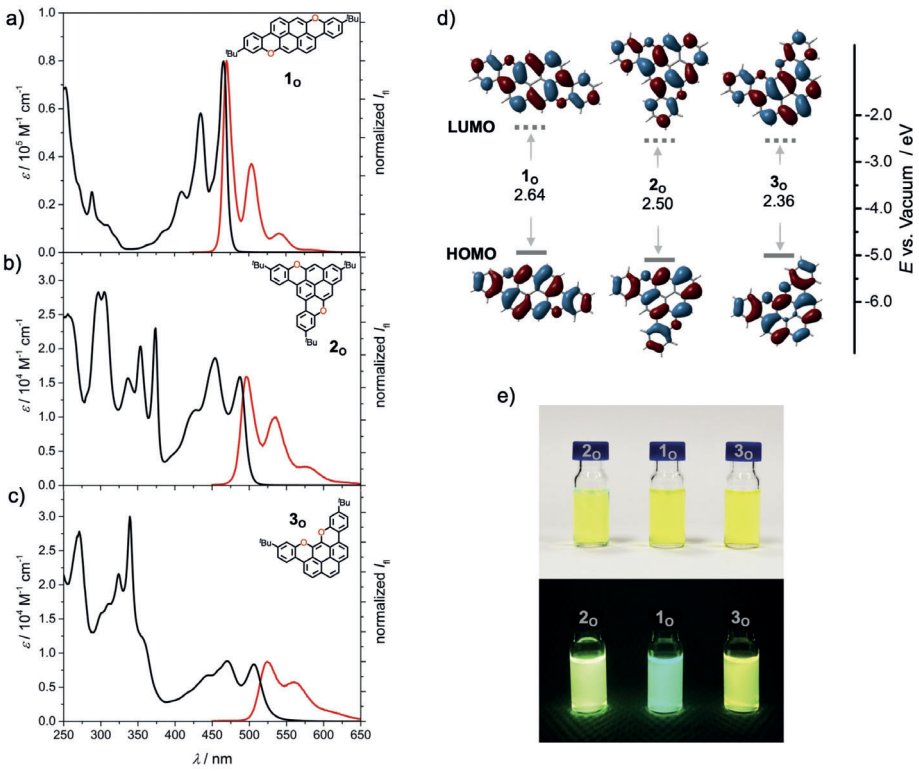

Figure 3. a)–c) UV/Vis absorption (black) and emission (red) spectra for $\mathbf{1_O}$–$\mathbf{3_O}$ in THF at room temperature. d) FMO energies obtained by CV (full) and E_{00} (dashed) along with Kohn–Sham wavefunctions calculated at B3LYP/6-31(d,p); the optical band gap shrinks in the order $\mathbf{1_O} > \mathbf{2_O} > \mathbf{3_O}$. e) Absorption and emission colors for $\mathbf{1_O}$–$\mathbf{3_O}$ in THF at room temperature.

Molecules $\mathbf{1_O}$, $\mathbf{2_O}$, and $\mathbf{3_O}$ show the lowest electronic transitions at 466, 487 and 506 nm, respectively, in the UV/Vis absorption spectra (Table 1, Figures 3 and S8), with the strongest absorptivity found for $\mathbf{1_O}$. As shown by TD-DFT calculations (Tables S20–S22, Figures S47,S49), these bands can be attributed to π–π* transitions. A comparison between the absorption profiles (in THF) of O-doped PAH $\mathbf{1_O}$ and the (only) previously reported full-carbon compound $\mathbf{1_C}$ reveals a blue-shift of the lowest-energy absorption maximum (from 586 to 466 nm for $\mathbf{1_C}$ and $\mathbf{1_O}$, respectively; Figure S10). The increase in the optical band gap is caused by the replacement of two benzenoid rings with (slightly) antiaromatic pyrano rings, which causes an increase of the LUMO energy (from DFT calculations: $E_{LUMO} = -2.80$ and -1.80 eV for $\mathbf{1_C}$ and $\mathbf{1_O}$, respectively), while the HOMO energy is barely affected ($E_{HOMO} = -4.85$ and -4.72 eV for $\mathbf{1_C}$ and $\mathbf{1_O}$, respectively). Emission profiles for $\mathbf{1_O}$, $\mathbf{2_O}$, and $\mathbf{3_O}$ displayed mirroring luminescence profiles with narrow Stokes shifts (4, 9, and 18 nm, respectively), high quantum yields ($\Phi_{fl} = 93$, 88, and 68 %, respectively) and short lifetimes ($\tau = 2.2$, 6.2, and 6.2 ns, respectively).

Cyclic voltammetry (CV) was used to assess the redox properties in THF (Table 1, Figures S11–S13). The CV profiles of $\mathbf{1_O}$ and $\mathbf{3_O}$ feature two reversible oxidation couples (0.10 and 0.54 V for $\mathbf{1_O}$; 0.15 and 0.54 V for $\mathbf{3_O}$), whereas only one reversible oxidation event was detected for $\mathbf{2_O}$ at 0.29 V, together with an irreversible process at 0.72 V. Only irreversible reduction waves were observed in the redox window of THF (Figures S11–S13). By comparing the diffusion coefficients measured for $\mathbf{1_O}$, $\mathbf{2_O}$ and $\mathbf{3_O}$ by DOSY-NMR (1.10×10^{-5}, 9.89×10^{-6}, and 1.11×10^{-5} $cm^2 s^{-1}$, respectively) with those obtained from the first cathodic events (1.24×10^{-5}, 9.55×10^{-6}, and 1.13×10^{-5} $cm^2 s^{-1}$, measured at 0.18, 0.34, and 0.20 V, respectively), we could assert that the first oxidation waves correspond to the formation of the radical cation species ($\mathbf{1_O}^{\bullet+}$, $\mathbf{2_O}^{\bullet+}$, and $\mathbf{3_O}^{\bullet+}$; see Section S5 in the Supporting Information). These findings suggest that all oxidation states are likely accessible by titration with tris(4-bromophenyl)ammoniumyl hexafluoroantimonate ($BAHA_F$), a one-electron oxidant ($E^{red} = 0.70$ V vs. Fc/Fc^+).[19]

The effects of oxidation are particularly apparent in EPR spec-

Table 1: Optoelectronic properties of $\mathbf{1_O}$–$\mathbf{3_O}$ in air-equilibrated THF. Half-wave potentials ($E_{1/2}$) determined by CV (THF, 0.1 M n-Bu_4NPF_6) and referenced versus Fc^+/Fc couple.

molecule	λ_{abs} [nm]	λ_{em} [nm]	ϕ_{fl}[a] [%]	E_{00}[b] [eV]	E_{ac}^{red}[c] [V]	$E_{1/2}^{ox1}$ [V]	$E_{1/2}^{ox1}$ [V]	E_{HOMO}[e] [eV]	E_{LUMO}[f] [eV]
$\mathbf{1_O}$	466	470	93	2.64	−2.54	0.10	0.54	−4.90	−2.26
$\mathbf{2_O}$	487	496	88	2.50	−2.42	0.29	0.72[d]	−5.09	−2.59
$\mathbf{3_O}$	506	524	68	2.36	−2.02	0.15	0.54	−4.95	−2.59

[a] ϕ_{fl} measured by the optical dilute method and Coumarin 153 as reference. [b] Optical band gap. [c] From the cathodic peak of an irreversible process. [d] From the anodic peak of an irreversible process. [e] The formal potential of the Fc^+/Fc couple is assumed to be −4.8 eV vs. vacuum. [f] Calculated using E_{00}.

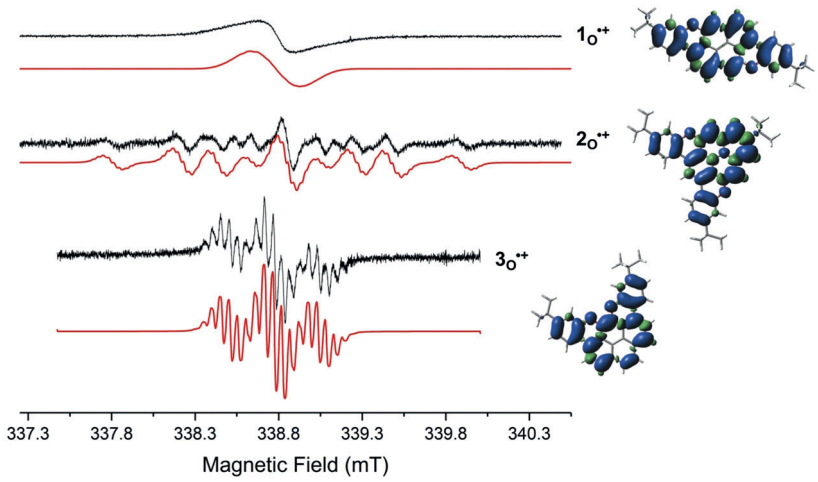

Figure 4. Left: X-band CW-EPR spectra (black) and simulations (red) of radical cations $\mathbf{1_O}^{\bullet+}$, $\mathbf{2_O}^{\bullet+}$, and $\mathbf{3_O}^{\bullet+}$ in THF solutions, generated with $BAHA_F$. Right: Corresponding spin-density distribution maps calculated at UB3LYP/EPR-II.

tra if unpaired electrons are present. Titration of one equiv $BAHA_F$ into solutions of $\mathbf{1_O}$, $\mathbf{2_O}$, and $\mathbf{3_O}$ gave the corresponding radical cations $\mathbf{1_O}^{\bullet+}$, $\mathbf{2_O}^{\bullet+}$, and $\mathbf{3_O}^{\bullet+}$, with the latter exhibiting X-band CW-EPR signals characteristic of $S = 1/2$ electron-spin systems (Figure 4). The isotropic g_{iso} and $^{H}a_{iso}$ values show agreement with theoretical estimates (Table S5). Upon further addition of $BAHA_F$ (> 1 equiv), the intensity of the EPR signals decreased until complete disappearance (> 2 equiv), and this coincided with the emergence of the EPR signal of $BAHA_F$. For instance, the closed-shell EPR-silent cations $\mathbf{1_O}^{2+}$ and $\mathbf{3_O}^{2+}$ are obtained in the case of $\mathbf{1_O}$ and $\mathbf{3_O}$ (Figure S35). Given the irreversibility of the second oxidation process for $\mathbf{2_O}$, we did not perform any EPR characterization for this molecule in the presence of an excess of $BAHA_F$. To shed further light on the properties of the oxidized species, we also performed UV/Vis–NIR spectroelectrochemical (Figures S17–S20) and spectrophotometric titration experiments with both BAHA (magic blue) and $BAHA_F$ (Figures 5 and S21–S24). In all cases, the absorption spectra readily underwent drastic changes with a progressive disappearance of the electronic transitions at 410–510 nm and the simultaneous appearance of new red-shifted bands in the NIR spectral region, typical of radical-cation species. We further attempted to characterize the dications in solution by ^{1}H NMR spectroscopy (Figures S25–S28). While we observed the disappearance of signals from the neutral species accompanied by the appearance of new proton resonances upon addition of BAHA, the interpretation was complicated by the evident loss of intensity, presumably due to the strong tendency of the oxidized species to aggregate (Figure S28). Moreover, all attempts to obtain single crystals of the chemically oxidized species suitable for X-ray diffraction were unsuccessful.

The formation of the cationic species was further corroborated by DFT calculations and their aromaticity was probed by nucleus-independent chemical shift (NICS) and anisotropy of the induced current density (AICD) analyses (Supporting Information, Section S11).[20] $NICS(1)_{zz}$ values (Figures S54–S57) of the pyrano rings show antiaromatic

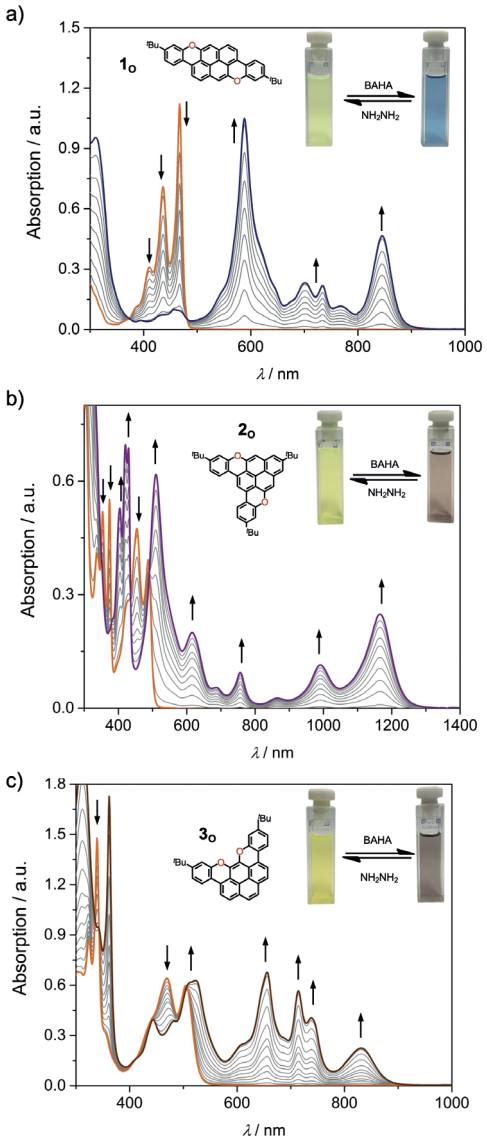

Figure 5. UV/Vis–NIR spectra obtained by titration of a) $\mathbf{1_O}$, b) $\mathbf{2_O}$, and c) $\mathbf{3_O}$ with BAHA (magic blue) in dry CH_2Cl_2 at 298 K.

character (+12.76, +10.93, and +14.66 ppm for $\mathbf{1_O}$, $\mathbf{2_O}$, and $\mathbf{2_O}$, respectively), while one-electron oxidation results in that ring becoming essentially non-aromatic (−1.18, +0.73, and +0.30 ppm, respectively) and double-oxidation gives pyrylium rings with aromatic character (−18.06, −6.54, and −17.11 ppm, respectively), similar to the all-carbon neutral PAH counterparts $\mathbf{1_C}$–$\mathbf{3_C}$ (Figures S58,S59). In contrast to typical C–O single bonds (1.43 Å), the newly formed C–O bonds (Figures S44–S46) are substantially shorter (1.37 Å) in the neutral $\mathbf{1_O}$–$\mathbf{3_O}$ species, suggesting that the non-bonding electron pairs at the oxygen atoms contribute to the π-extension of the PAH. The C–O bonds were observed to shorten even further in the calculated oxidized O-PAHs (1.35 Å for the radical cations and 1.33–1.34 Å for the dications). TD-DFT simulations (Tables S25–S30, Figure S50) of the UV/Vis absorption bands resembled the experimentally observed ones for the oxidized species.

We then turned our attention to the electrocrystallization technique[21] in order to grow crystals of the cations suitable for X-ray diffraction and perform electrooxidation experiments (Supporting Information, Section S8). Triclinic shiny black crystals containing salts of MV complexes of the O-doped PAHs $\mathbf{1_O}$ and $\mathbf{3_O}$ were obtained in THF with *n*-Bu_4NPF_6 and *n*-Bu_4NClO_4 as electrolytes, respectively (Figure 6). While $\mathbf{1_O}$ electro-crystallizes in an asymmetric unit containing ten crystallographically independent molecules, six PF_6^- anions, and 16 solvent molecules $[(\mathbf{1_O})_{10}(PF_6)_6{\cdot}(THF)_{16}]$, $\mathbf{3_O}$ features three independent molecules, two ClO_4^- anions, one THF, and half an H_2O molecule in the asymmetric unit $[(\mathbf{3_O})_3(ClO_4)_2{\cdot}THF{\cdot}0.5\,H_2O]$. All attempts to grow suitable crystals containing the oxidized species of $\mathbf{2_O}$ for X-ray analyses failed.

Looking the solid-state structure of $(\mathbf{1_O})_{10}(PF_6)_6{\cdot}(THF)_{16}$ (Figure 6a_1–d_1), a columnar arrangement in which the molecules organize antiparallelly is clearly evident (Figure 6b_1), with an average interplanar spacing of 3.33(7) Å (shortest distance between ring centroids: 3.367(12) Å with a lateral slippage of 0.83 Å). The PF_6^- counterions are evenly intercalated in the channels (Figure 4c_1) together with THF solvent molecules. Similarly, in the crystal structure of $(\mathbf{3_O})_3(ClO_4)_2{\cdot}THF{\cdot}0.5\,H_2O$ (Figure 6a_2–d_2), molecule $\mathbf{3_O}$ forms π-stacks (π–π distances from 3.21 to 3.42 Å, Figure 6c_2), with ClO_4^- anions and solvent molecules intercalating between different stacks. In this crystal, two stacking modes are

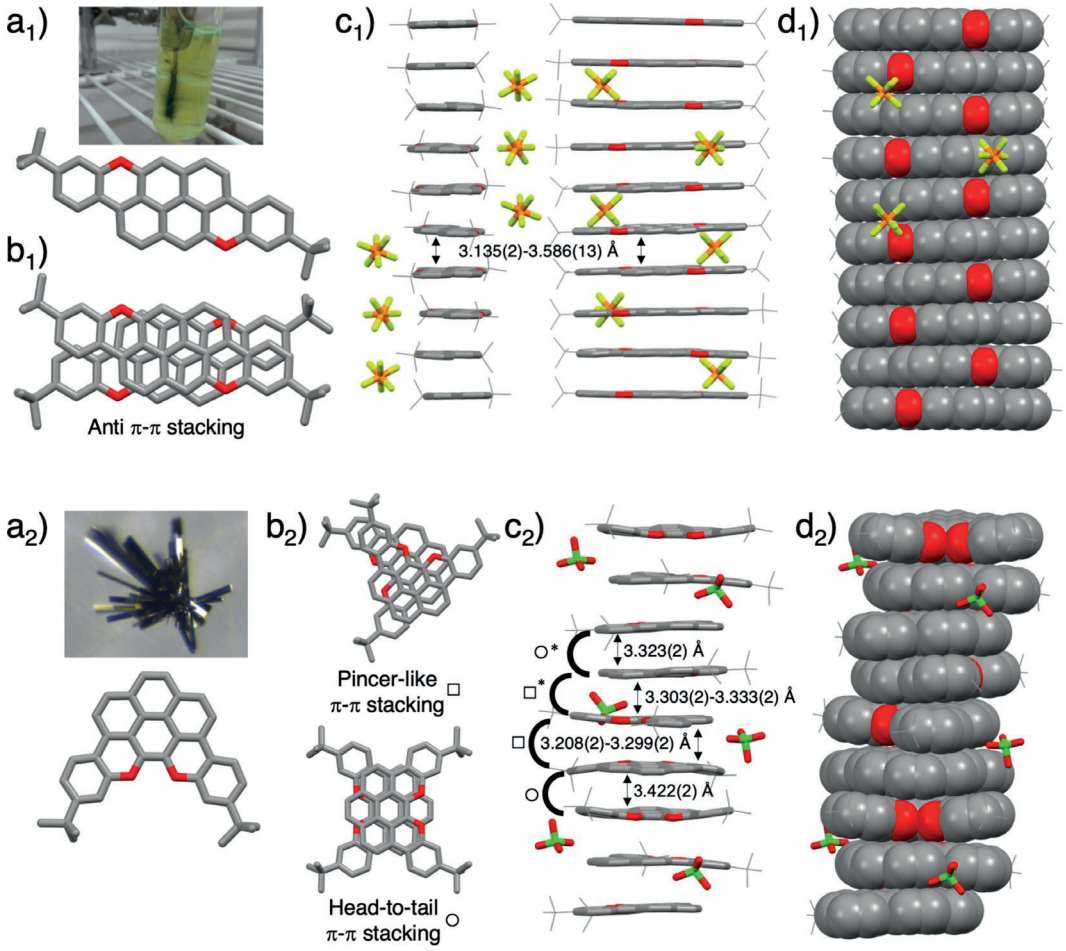

Figure 6. X-ray crystal structures for the MV complexes $(\mathbf{1_O})_{10}(PF_6)_6{\cdot}(THF)_{16}$ (top, $P\bar{1}$) and $(\mathbf{3_O})_3(ClO_4)_2{\cdot}THF{\cdot}0.5\,H_2O$ (bottom, $P\bar{1}$). Solvent molecules omitted for clarity. a) Morphology of the crystals and X-ray structure of the relevant corresponding molecule, b) π-stacking mode, c), d) solid-state columnar π-stacks. For the MV complexes of $\mathbf{3_O}$, each stacking mode between two $\mathbf{3_O}$ molecules gives rise to two different offset arrangements (marked by an asterisk). Atom colors: red (O), gray (C), green (Cl), yellow (F), orange (P).

present: a pincer-like stack (Figure 6b$_2$, top), where two independent molecules are facing to each other in an antiparallel fashion with a relative angle of about 90°, and a head-to-tail arrangement (bottom), where two molecules stack antiparallelly. In both MV complexes, all O-doped PAHs show very similar bond lengths Table S4) and short interplanar π–π distances. These structures are consistent with a material in which the charge is delocalized over the stacks.[22] A MV salt would form a partially filled band structure enabling conduction.

As crystals for $(\mathbf{1_O})_{10}(PF_6)_6\cdot(THF)_{16}$ were extremely fragile, we used $(\mathbf{3_O})_3(ClO_4)_2\cdot THF\cdot 0.5\,H_2O$ to probe the electronic properties of the organic salts. We first performed variable-temperature (VT) X-band CW-EPR investigations (Figure 7a). The EPR spectra are constituted by what appears to be a (medium-polarized) conduction-electron-spin-resonance line, most likely associated with a delocalization of spin density along the long axis of the π-stacking architecture. This behavior has been observed in systems showing metal-to-insulator/semiconductor transitions.[23] Because the intensity of the EPR signal decreases when the temperature is lowered, an Arrhenius plot has been used to interpret the temperature-dependent EPR behavior (Figure 7a,b). The linear portion of the trend at low temperature was fitted to a line of equation $f(T) = -476\,T^{-1} + 8.77$ and an activation energy (E_a) of 4.1×10^{-2} eV was obtained, which is in good agreement with the value derived from single-crystal conductivity measurements.

Relaxation studies were also performed at 5, 10, and 15 K to calculate the phase-memory time t_m (that is, the transversal relaxation or spin–spin relaxation time t_2, Figure 7c). Already at 20 K, no Hahn echo was detected when using a primary π/2−π−π pulse sequence, even when shortening the inter-pulse delay, τ, to the minimum. A fast t_m value of 0.43 μs was measured at 5 K, which rapidly decreased to 0.34 μs and 0.29 μs at 10 K and 15 K, respectively. Notably, solid-state t_m values are ten times lower than those measured in frozen THF for the radical cation $\mathbf{3_O}^{\bullet+}$, that is, 4 μs at 5 K (Figure S37). Overall, these observations suggest that fast spin–spin relaxation routes occur in the crystal due to the stacking of the paramagnetic radical cations. Similarly, a short relaxation time t_1 (or longitudinal spin-lattice relaxation time) was measured (Figure S37). A decrease of the t_1 value as a function of the temperature was also observed (0.21 ms at 5 K, 0.07 ms at 10 K, and 0.05 ms at 15 K), which is 120 times lower than the t_1 value (25 ms) measured for $\mathbf{3_O}^{\bullet+}$ in solution. The drastic lowering of t_1 further corroborates the presence of an ordered crystal lattice in the electrochemically grown solid material.

I–V curves of single crystals of $(\mathbf{3_O})_3(ClO_4)_2\cdot THF\cdot 0.5\,H_2O$ exhibit a typical semiconductor behavior with a sigmoidal shape rather than a linear behavior, consistent with the observed temperature dependence of the conductivity (Figure 8a,b).[24] The conductivity (σ) was calculated in the ohmic region (σ_{ohmic}), that is, around zero bias, and, as an extension, in the non-ohmic ($\sigma_{non\text{-}ohmic}$) activated regime at higher bias values. Considering that organic materials are typically poorly conductive semiconductors ($\sigma < 10^{-6}$ S cm^{-1} at 300 K) or even insulators,[25] our mixed-valence crystalline complexes exhibit high conductivities at room temperature ($\sigma_{ohmic} = 8.8 \times 10^{-5}$ and 3.7×10^{-3} S cm^{-1} as well as $\sigma_{non\text{-}ohmic} = 2.4 \times 10^{-4}$ and 5.1×10^{-3} S cm^{-1} for crystals α and β, respectively, where α and β refer to two different crystals from the same batch). Exceptions include crystalline organic conductors and superconductors based on electron donors (such as TTF) and

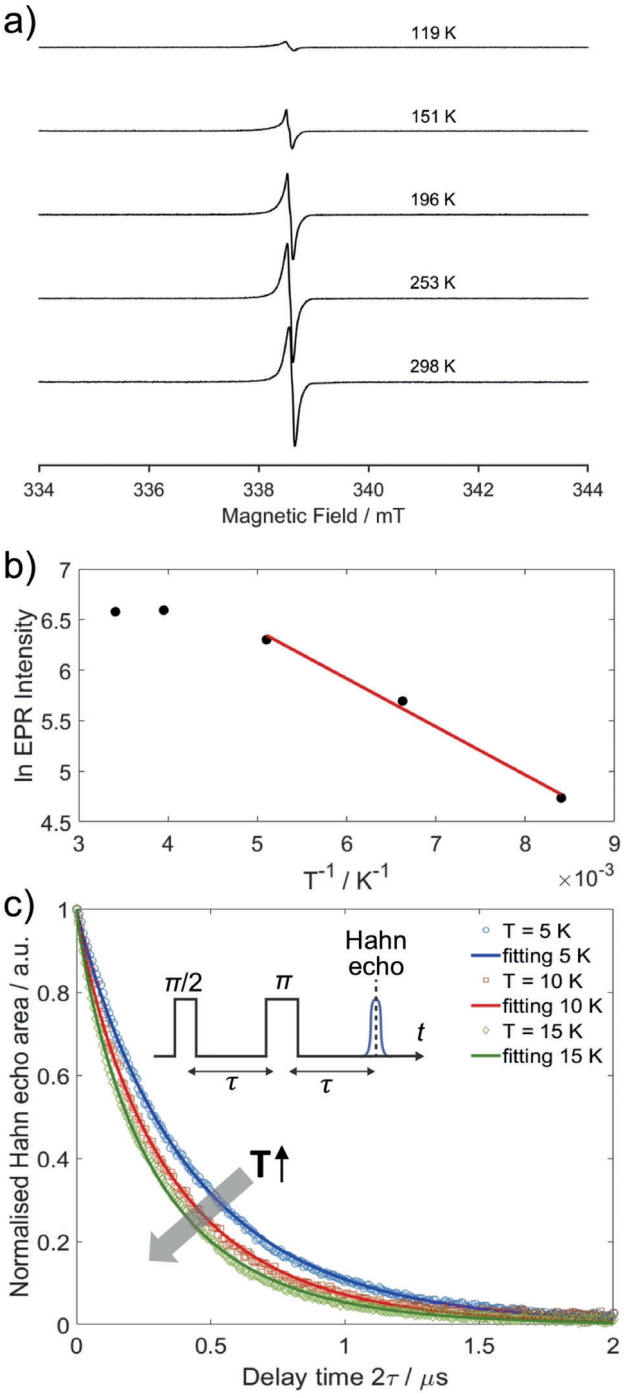

Figure 7. a) VT X-band CW-EPR spectra of crystals of $(\mathbf{3_O})_3(ClO_4)_2\cdot THF\cdot 0.5\,H_2O$ between 298 K and 119 K at 10 kHz field-modulation frequency; b) logarithm of the EPR intensity vs. 1/*T* (Arrhenius plot). $R^2 = 0.9933$; c) two-pulse Hahn-echo decay measured at 15 K (green), 10 K (red), and 5 K (blue). Inset: Pulse sequence adopted to generate a primary electron-spin echo. Microwave pulse lengths of π = 120 ns were used to suppress any potential proton–electron spin modulation.

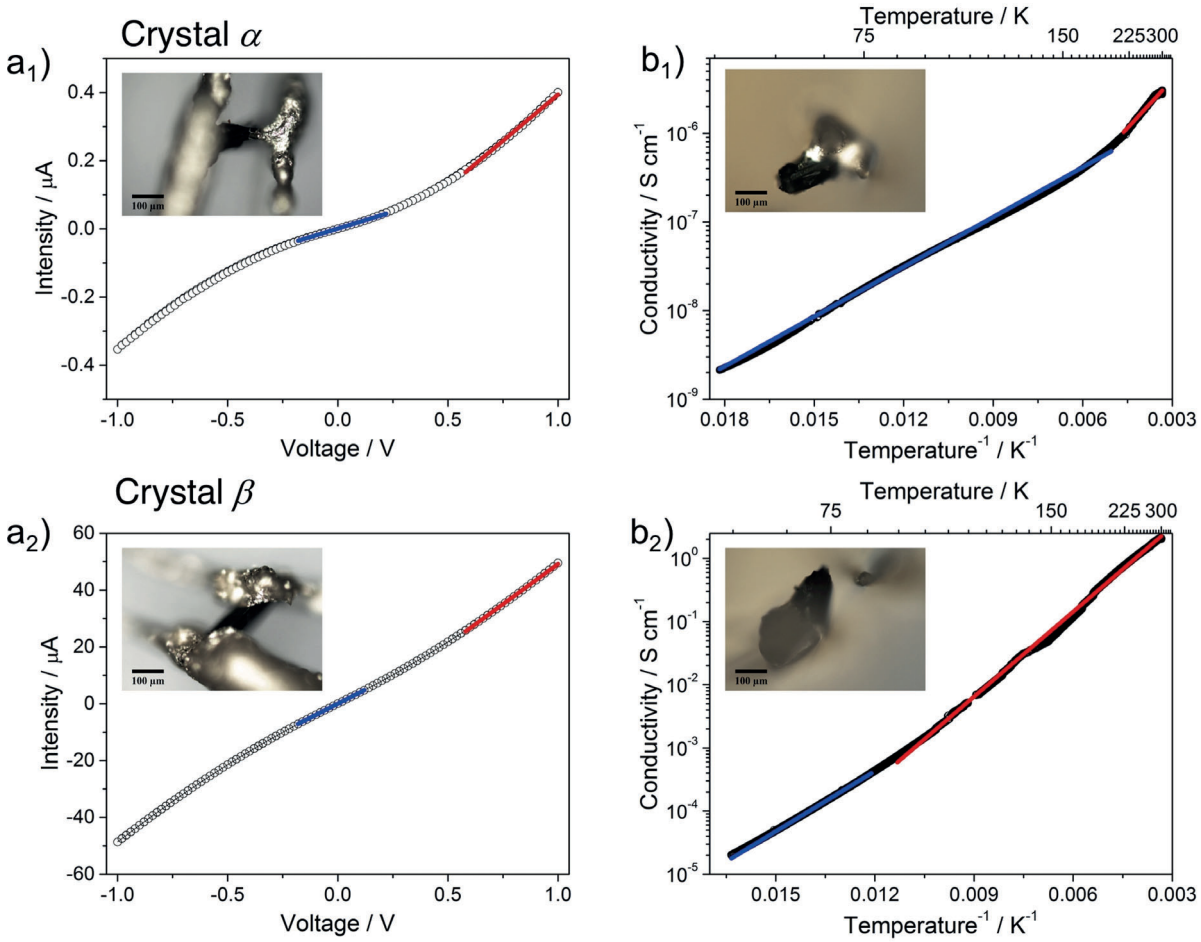

Figure 8. Device and electrical response of two crystals (α and β) of $(\mathbf{3_O})_3(ClO_4)_2$·THF·0.5 H_2O: a) *I*--*V* curve (white circles) at 300 K with the ohmic linear fit (blue) and non-ohmic fit (red). Crystal α: ohmic fit ($R^2 = 0.99752$) slope $1.98 \pm 0.02 \times 10^{-7}\ \Omega^{-1}$, *y*-intercept $9 \pm 2 \times 10^{-10}$ A; non-ohmic fit ($R^2 = 0.99752$) slope $5.43 \pm 0.01 \times 10^{-7}\ \Omega^{-1}$, *y*-intercept $-1.48 \pm 0.003 \times 10^{-7}$ A. Crystal β: ohmic fit ($R^2 = 0.99998$) slope $3.943 \pm 0.005 \times 10^{-5}\ \Omega^{-1}$, *y*-intercept $2 \pm 5 \times 10^{-9}$ A; non-ohmic fit ($R^2 = 0.99957$) slope $5.46 \pm 0.02 \times 10^{-5}\ \Omega^{-1}$, *y*-intercept $-7.26 \pm 0.0015 \times 10^{-6}$ A. b) Arrhenius plot of the conductivity vs. inverse temperature together with the linear fits (blue, red) in the low- and high-temperature regimes. Conductivity values calculated at high ($\sigma_{0,HT}$) and low ($\sigma_{0,LT}$) temperatures, same for the associated activation energies ($E_{a,HT}$ and $E_{a,LT}$). Crystal α: $\sigma_{0,HT} = 5.50 \pm 0.05$ S cm^{-1}, $E_{a,HT} = 72.0 \pm 0.6$ meV ($R^2 = 0.99359$); $\sigma_{0,LT} = 4.92 \pm 0.12 \times 10^{-6}$ S cm^{-1}, $E_{a,LT} = 37.15 \pm 0.14$ meV ($R^2 = 0.99915$). Crystal β: $\sigma_{0,HT} = 70.0 \pm 0.5$ S cm^{-1}, $E_{a,HT} = 80.21 \pm 0.09$ meV ($R^2 = 0.99817$); $\sigma_{0,LT} = 2.81 \pm 0.08 \times 10^{-6}$ S cm^{-1}, $E_{a,LT} = 63.11 \pm 0.07$ meV ($R^2 = 0.99967$). Insets: top view (a) and lateral view (b) of the devices.

acceptors (such as TCNQ),[26] some organic and inorganic radicals,[27] and some metal-organic frameworks (MOFs).[28]

Conclusion

In summary, we have developed an efficient synthesis for the construction of O-embedded PAHs. This approach consists in long-axis or short-axis extension of dihalogenated pyrenes, which, coupled with phenol moieties, can be planarized through oxidative Pummerer ring-closure (CuO in $PhNO_2$). Electrochemical and chemical-oxidation investigations showed that the cations of the O-PAHs are easily accessible, prompting us to perform electrocrystallization experiments to form organic MV crystals. The organic salts organize in columns in the solid state, showing a strong electron delocalization along the long axis of the π-stacks. Electric measurements of single crystals of the MV salts exhibited a semiconducting behavior with relatively high conductivity at room temperature, further supporting the idea that the heteroatom approach is a viable route for endowing PAHs and nanographenes with a broad spectrum of semiconducting properties and high charge mobilities.

Acknowledgements

D.B. gratefully acknowledge the EU through the ERC Starting Grant "COLORLANDS", the MC-RISE "INFUSION" and MC-ITN "PHOTOTRAIN" projects and the School of Chemistry at Cardiff University for financial support. The work in Spain has been financed by the MINECO (grants MAT2017-89993-R and Excellence Unit María de Maeztu MDM-2015-0538) and the Generalidad Valenciana (Prometeo Programme). The authors thank Prof. R. Herges (Kiel University) for providing the AICD program,

Prof. A. Stanger (Technion Israel institute of Technology) for sharing the Aroma package and Dr. A. Fermi (Cardiff University) for the spectro-electrochemical measurements.

Conflict of interest

The authors declare no conflict of interest.

Keywords: electrocrystallization · electron paramagnetic resonance · heteroatom doping · molecular graphenes · polycyclic aromatic hydrocarbons

[1] a) L. Chen, Y. Hernandez, X. Feng, K. Müllen, *Angew. Chem. Int. Ed.* **2012**, *51*, 7640 – 7654; *Angew. Chem.* **2012**, *124*, 7758 – 7773; b) A. Narita, X. Y. Wang, X. Feng, K. Müllen, *Chem. Soc. Rev.* **2015**, *44*, 6616 – 6643; c) Y. Segawa, H. Ito, K. Itami, *Nat. Rev. Mater.* **2016**, *1*, 15002.

[2] a) L. Zhang, Y. Cao, N. S. Colella, Y. Liang, J. L. Bredas, K. N. Houk, A. L. Briseno, *Acc. Chem. Res.* **2015**, *48*, 500 – 509; b) T. B. Schon, B. T. McAllister, P.-F. Li, D. S. Seferos, *Chem. Soc. Rev.* **2016**, *45*, 6345 – 6404; c) P. Mayorga Burrezo, W. Zeng, M. Moos, M. Holzapfel, S. Canola, F. Negri, C. Rovira, J. Veciana, H. Phan, J. Wu, C. Lambert, J. Casado, *Angew. Chem. Int. Ed.* **2019**, *58*, 14467 – 14471; *Angew. Chem.* **2019**, *131*, 14609 – 14613.

[3] a) X. Wang, G. Sun, P. Routh, D. H. Kim, W. Huang, P. Chen, *Chem. Soc. Rev.* **2014**, *43*, 7067 – 7098; b) M. Stępień, E. Gońka, M. Żyła, N. Sprutta, *Chem. Rev.* **2017**, *117*, 3479 – 3716; c) R. Szűcs, P.-A. Bouit, L. Nyulászi, M. Hissler, *ChemPhysChem* **2017**, *18*, 2618 – 2630; d) M. Hirai, N. Tanaka, M. Sakai, S. Yamaguchi, *Chem. Rev.* **2019**, *119*, 8291 – 8331.

[4] a) S. Yamaguchi in *Chemical Science of π-Electron Systems* (Eds.: T. Akasaka, A. Osuka, S. Fukuzumi, H. Kandori, Y. Aso), Springer Japan, Tokyo, **2015**, pp. 363 – 377 (https://doi.org/10.1007/978-974-431-55357-1_21); b) D. Bonifazi, F. Fasano, M. M. Lorenzo-García, D. Marinelli, H. Oubaha, J. Tasseroul, *Chem. Commun.* **2015**, *51*, 15222 – 15236; c) H. Helten, *Chem. Eur. J.* **2016**, *22*, 12972 – 12982; d) M. M. Morgan, W. E. Piers, *Dalton Trans.* **2016**, *45*, 5920 – 5924; e) A. John, M. Bolte, H. W. Lerner, M. Wagner, *Angew. Chem. Int. Ed.* **2017**, *56*, 5588 – 5592; *Angew. Chem.* **2017**, *129*, 5680 – 5684; f) J. M. Farrell, D. Schmidt, V. Grande, F. Würthner, *Angew. Chem. Int. Ed.* **2017**, *56*, 11846 – 11850; *Angew. Chem.* **2017**, *129*, 12008 – 12012; g) R. J. Kahan, D. L. Crossley, J. Cid, J. E. Radcliffe, M. J. Ingleson, *Angew. Chem. Int. Ed.* **2018**, *57*, 8084 – 8088; *Angew. Chem.* **2018**, *130*, 8216 – 8220; h) H. Noda, Y. Asada, M. Shibasaki, N. Kumagai, *J. Am. Chem. Soc.* **2019**, *141*, 1546 – 1554; i) M. Vanga, R. A. Lalancette, F. Jakle, *Chem. Eur. J.* **2019**, *25*, 10133 – 10140.

[5] a) D. B. Granger, Y. Mei, K. J. Thorley, S. R. Parkin, O. D. Jurchescu, J. E. Anthony, *Org. Lett.* **2016**, *18*, 6050 – 6053; b) Y. S. Park, D. J. Dibble, J. Kim, R. C. Lopez, E. Vargas, A. A. Gorodetsky, *Angew. Chem. Int. Ed.* **2016**, *55*, 3352 – 3355; *Angew. Chem.* **2016**, *128*, 3413 – 3416; c) D. Lehnherr, J. M. Alzola, C. R. Mulzer, S. J. Hein, W. R. Dichtel, *J. Org. Chem.* **2017**, *82*, 2004 – 2010; d) L. Ji, A. Friedrich, I. Krummenacher, A. Eichhorn, H. Braunschweig, M. Moos, S. Hahn, F. L. Geyer, O. Tverskoy, J. Han, C. Lambert, A. Dreuw, T. B. Marder, U. H. F. Bunz, *J. Am. Chem. Soc.* **2017**, *139*, 15968 – 15976; e) Z. Zeng, H. Jin, K. Sekine, M. Rudolph, F. Rominger, A. S. K. Hashmi, *Angew. Chem. Int. Ed.* **2018**, *57*, 6935 – 6939; *Angew. Chem.* **2018**, *130*, 7051 – 7056; f) P. Karak, C. Dutta, T. Dutta, A. L. Koner, J. Choudhury, *Chem. Commun.* **2019**, *55*, 6791 – 6794; g) U. H. F. Bunz, J. Freudenberg, *Acc. Chem. Res.* **2019**, *52*, 1575 – 1587; h) C. L. Deng, J. P. Bard, L. N. Zakharov, D. W. Johnson, M. M. Haley, *Org. Lett.* **2019**, *21*, 6427 – 6431; i) B. L. Hu, C. An, M. Wagner, G. Ivanova, A. Ivanova, M. Baumgarten, *J. Am. Chem. Soc.* **2019**, *141*, 5130 – 5134; j) J. P. Mora-Fuentes, A. Riaño, D. Cortizo-Lacalle, A. Saeki, M. Melle-Franco, A. Mateo-Alonso, *Angew. Chem. Int. Ed.* **2019**, *58*, 552 – 556; *Angew. Chem.* **2019**, *131*, 562 – 566.

[6] a) D. Wu, W. Pisula, M. C. Haberecht, X. Feng, K. Müllen, *Org. Lett.* **2009**, *11*, 5686 – 5689; b) S. Shinamura, E. Miyazaki, K. Takimiya, *J. Org. Chem.* **2010**, *75*, 1228 – 1234; c) K. P. Rao, M. Kondo, R. Sakamoto, T. Kusamoto, M. Nishikawa, S. Kume, M. Nihei, H. Oshio, H. Nishihara, *Chem. Eur. J.* **2011**, *17*, 14010 – 14019; d) M. Nakano, K. Niimi, E. Miyazaki, I. Osaka, K. Takimiya, *J. Org. Chem.* **2012**, *77*, 8099 – 8111; e) B. Vanveller, D. Robinson, T. M. Swager, *Angew. Chem. Int. Ed.* **2012**, *51*, 1182 – 1186; *Angew. Chem.* **2012**, *124*, 1208 – 1212; f) S. Wang, B. Lv, Q. Cui, X. Ma, X. Ba, J. Xiao, *Chem. Eur. J.* **2015**, *21*, 14791 – 14796; g) D. Stassen, N. Demitri, D. Bonifazi, *Angew. Chem. Int. Ed.* **2016**, *55*, 5947 – 5951; *Angew. Chem.* **2016**, *128*, 6051 – 6055; h) T. Miletić, A. Fermi, I. Orfanos, A. Avramopoulos, F. De Leo, N. Demitri, G. Bergamini, P. Ceroni, M. G. Papadopoulos, S. Couris, D. Bonifazi, *Chem. Eur. J.* **2017**, *23*, 2363 – 2378; i) A. Berezin, N. Biot, T. Battisti, D. Bonifazi, *Angew. Chem. Int. Ed.* **2018**, *57*, 8942 – 9084; *Angew. Chem.* **2018**, *130*, 9080 – 9084; j) A. Sciutto, A. Fermi, A. Folli, T. Battisti, J. Beames, D. Murphy, D. Bonifazi, *Chem. Eur. J.* **2018**, *24*, 4382 – 4389; k) A. Sciutto, A. Berezin, M. Lo Cicero, T. Miletić, A. Stopin, D. Bonifazi, *J. Org. Chem.* **2018**, *83*, 13787 – 13798; l) C. Li, L. Zhu, W. Liang, R. Su, J. Yin, Y. Hu, Y. Lan, D. Wu, J. You, *Chem. Sci.* **2019**, *10*, 7274 – 7280; m) S. Dong, T. Y. Gopalakrishna, Y. Han, H. Phan, T. Tao, Y. Ni, G. Liu, C. Chi, *J. Am. Chem. Soc.* **2019**, *141*, 62 – 66; n) H. Wu, H. Fan, S. Chen, C. Yang, L. Ye, H. Ade, *Small* **2019**, *15*, 1902656; o) L. Yang, M. Li, J. Song, Y. Zhou, Z. Bo, H. Wang, *Adv. Funct. Mater.* **2018**, *28*, 1705927; p) C. W. Lee, J. A. Seo, M. S. Gong, J. Y. Lee, *Chem. Eur. J.* **2013**, *19*, 1194 – 1198.

[7] a) P. Ruffieux, S. Wang, B. Yang, C. Sánchez-Sánchez, J. Liu, T. Dienel, L. Talirz, P. Shinde, C. A. Pignedoli, D. Passerone, T. Dumslaff, X. Feng, K. Müllen, R. Fasel, *Nature* **2016**, *531*, 489 – 492; b) X. Wang, F. Zhang, K. S. Schellhammer, P. Machata, F. Ortmann, G. Cuniberti, Y. Fu, J. Hunger, R. Tang, A. A. Popov, R. Berger, K. Müllen, X. Feng, *J. Am. Chem. Soc.* **2016**, *138*, 11606 – 11615; c) M. Numano, N. Nagami, S. Nakatsuka, T. Katayama, K. Nakajima, S. Tatsumi, N. Yasuda, T. Hatakeyama, *Chem. Eur. J.* **2016**, *22*, 11574 – 11577; d) M. Fingerle, C. Maichle-Mössmer, S. Schundelmeier, B. Speiser, H. F. Bettinger, *Org. Lett.* **2017**, *19*, 4428 – 4431.

[8] a) F. Pina, M. J. Melo, C. A. Laia, A. J. Parola, J. C. Lima, *Chem. Soc. Rev.* **2012**, *41*, 869 – 908; b) F. Pina, *Dyes Pigm.* **2014**, *102*, 308 – 314.

[9] a) O. Anamimoghadam, M. D. Symes, D. L. Long, S. Sproules, L. Cronin, G. Bucher, *J. Am. Chem. Soc.* **2015**, *137*, 14944 – 14951; b) C. M. Wehrmann, R. T. Charlton, M. S. Chen, *J. Am. Chem. Soc.* **2019**, *141*, 3240 – 3248; c) Y. Wang, S. Qiu, S. Xie, L. Zhou, Y. Hong, J. Chang, J. Wu, Z. Zeng, *J. Am. Chem. Soc.* **2019**, *141*, 2169 – 2176.

[10] a) T. S. Balaban, A. T. Balaban in *Six-membered Hetarenes with one Chalcogen*, *Vol. 14* (Ed.: E. J. Thomas), Georg Thieme, Stuttgart, **2003**, pp. 11 – 200; b) J. Yin, M. Tan, D. Wu, R. Jiang, C. Li, J. You, *Angew. Chem. Int. Ed.* **2017**, *56*, 13094 – 13098; *Angew. Chem.* **2017**, *129*, 13274 – 13278.

[11] a) E. Clar, *Ber. Dtsch. Chem. Ges.* **1943**, *76*, 328 – 333; b) D. Lungerich, O. Papaianina, M. Feofanov, J. Liu, M. Devarajulu, S. I. Troyanov, S. Maier, K. Amsharov, *Nat. Commun.* **2018**, *9*, 4756.

[12] a) C. Reus, M. P. Lechner, M. Schulze, D. Lungerich, C. Diner, M. Gruber, J. M. Stryker, F. Hampel, N. Jux, R. R. Tykwinski, *Chem. Eur. J.* **2016**, *22*, 9097 – 9101; b) K. Sbargoud, M. Mamada, T. Jousselin-Oba, Y. Takeda, S. Tokito, A. Yassar, J. Marrot, M. Frigoli, *Chem. Eur. J.* **2017**, *23*, 5076 – 5080.

[13] J. Hwang, M. Pototschnig, R. Lettow, G. Zumofen, A. Renn, S. Götzinger, V. Sandoghdar, *Nature* **2009**, *460*, 76 – 80.

[14] P. Siyushev, G. Stein, J. Wrachtrup, I. Gerhardt, *Nature* **2014**, *509*, 66 – 70.

[15] B. Yang, J. B. Trebbia, R. Baby, P. Tamarat, B. Lounis, *Nat. Photonics* **2015**, *9*, 658 – 662.

[16] a) R. Pummerer, E. Prell, A. Rieche, *Ber. Dtsch. Chem. Ges. A/B* **1926**, *59*, 2159 – 2161; b) R. Pummerer, A. Rieche, *Ber. Dtsch. Chem. Ges. A/B* **1926**, *59*, 2161 – 2175.

[17] A. Rossignon, D. Bonifazi, *Synthesis* **2019**, *51*, 3588 – 3599.

[18] a) T. Kaposi, S. Joshi, T. Hoh, A. Wiengarten, K. Seufert, M. Paszkiewicz, F. Klappenberger, D. Écija, L. Đorđević, T. Marangoni, D. Bonifazi, J. V. Barth, W. Auwärter, *ACS Nano* **2016**, *10*, 7665 – 7674; b) L. Đorđević, T. Marangoni, M. Liu, R. De Zorzi, S. Geremia, A. Minoia, R. Lazzaroni, Y. Ishida, D. Bonifazi, *ChemPlusChem* **2019**, *84*, 1270 – 1278.

[19] a) B. K. Bandlish, H. J. Shine, *J. Org. Chem.* **1977**, *42*, 561 – 563; b) N. G. Connelly, W. E. Geiger, *Chem. Rev.* **1996**, *96*, 877 – 910.

[20] a) P. v. R. Schleyer, C. Maerker, A. Dransfeld, H. Jiao, N. J. R. van Eikema Hommes, *J. Am. Chem. Soc.* **1996**, *118*, 6317 – 6318; b) D. Geuenich, K. Hess, F. Köhler, R. Herges, *Chem. Rev.* **2005**, *105*, 3758 – 3772.

[21] P. Batail, K. Boubekeur, M. Fourmigué, J.-C. P. Gabriel, *Chem. Mater.* **1998**, *10*, 3005 – 3015.

[22] C. Kröhnke, V. Enkelmann, G. Wegner, *Angew. Chem. Int. Ed. Engl.* **1980**, *19*, 912 – 919; *Angew. Chem.* **1980**, *92*, 941 – 942.

[23] F. Mehran, B. A. Scott, *Phys. Rev. Lett.* **1973**, *31*, 1347 – 1349.

[24] G. Givaja, P. Amo-Ochoa, C. J. Gómez-García, F. Zamora, *Chem. Soc. Rev.* **2012**, *41*, 115 – 147.

[25] T. Murata, C. Yamada, K. Furukawa, Y. Morita, *Commun. Chem.* **2018**, *1*, 47.

[26] a) E. Coronado, P. Day, *Chem. Rev.* **2004**, *104*, 5419 – 5448; b) P. Batail, *Chem. Rev.* **2004**, *104*, 4887 – 4890.

[27] a) Y. Le Gal, T. Roisnel, P. Auban-Senzier, N. Bellec, J. Íñiguez, E. Canadell, D. Lorcy, *J. Am. Chem. Soc.* **2018**, *140*, 6998 – 7004; b) M. A. Christensen, C. R. Parker, T. J. Sørensen, S. de Graaf, T. J. Morsing, T. Brock-Nannestad, J. Bendix, M. M. Haley, P. Rapta, A. Danilov, S. Kubatkin, O. Hammerich, M. B. Nielsen, *J. Mater. Chem. C* **2014**, *2*, 10428 – 10438.

[28] L. Sun, M. G. Campbell, M. Dincă, *Angew. Chem. Int. Ed.* **2016**, *55*, 3566 – 3579; *Angew. Chem.* **2016**, *128*, 3628 – 3642.

[29] CCDC 1557894, 1920493, 1557895, 1557896, 1912053 and 1936956 ($\mathbf{1_O}$, $\mathbf{5}$, $\mathbf{2_O}\cdot{}^1/_3\,CH_2Br_2$, $\mathbf{3_OCl_2}\cdot 0.2\,CH_2Br_2$, $(\mathbf{1_O})_{10}(PF_6)_6\cdot(THF)_{16}$, $(\mathbf{3_O})_3(ClO_4)_2\cdot THF\cdot 0.5\,H_2O$) contain the supplementary crystallographic data for this paper. These data can be obtained free of charge from The Cambridge Crystallographic Data Centre.

Nanographenes

L. Đorđević, C. Valentini, N. Demitri, C. Mézière, M. Allain, M. Sallé, A. Folli, D. Murphy, S. Mañas-Valero, E. Coronado, D. Bonifazi* ___ ■■■–■■■

O-Doped Nanographenes: The Pyrano/Pyrylium Route Towards Semiconducting Cationic Mixed-Valence Complexes

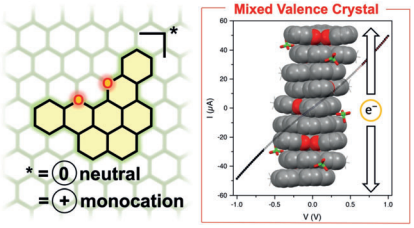

My O my! O-doped nanographenes derived from the π-extension of pyrene are reported. The compounds are highly fluorescent and feature low oxidation potentials. Electric measurements of single crystals of mixed-valence salts show a semiconducting behavior with a remarkably high conductivity at room temperature.